







Complementary *Operando* Spectroscopy identification of in-situ generated metastable charge-asymmetry $\text{Cu}_2\text{-CuN}_3$ clusters for CO_2 reduction to ethanol

Xiaozhi Su ^{1,7}, Zhuoli Jiang^{2,3,7}, Jing Zhou^{4,7}, Hengjie Liu ⁵, Danni Zhou², Huishan Shang², Xingming Ni⁶, Zheng Peng⁶, Fan Yang ⁶, Wenxing Chen ^{2✉}, Zeming Qi⁵, Dingsheng Wang ³ & Yu Wang ^{1✉}

Copper-based materials can reliably convert carbon dioxide into multi-carbon products but they suffer from poor activity and product selectivity. The atomic structure-activity relationship of electrocatalysts for the selectivity is controversial due to the lacking of systemic multiple dimensions for *operando* condition study. Herein, we synthesized high-performance CO_2RR catalyst comprising of CuO clusters supported on N-doped carbon nanosheets, which exhibited high C_{2+} products Faradaic efficiency of 73% including decent ethanol selectivity of 51% with a partial current density of 14.4 mA/cm^{-2} at -1.1 V vs. RHE. We evidenced catalyst restructuring and tracked the variation of the active states under reaction conditions, presenting the atomic structure-activity relationship of this catalyst. *Operando* XAS, XANES simulations and Quasi-in-situ XPS analyses identified a reversible potential-dependent transformation from dispersed CuO clusters to $\text{Cu}_2\text{-CuN}_3$ clusters which are the optimal sites. This cluster can't exist without the applied potential. The N-doping dispersed the reduced Cu_n clusters uniformly and maintained excellent stability and high activity with adjusting the charge distribution between the Cu atoms and N-doped carbon interface. By combining *Operando* FTIR and DFT calculations, it was recognized that the $\text{Cu}_2\text{-CuN}_3$ clusters displayed charge-asymmetric sites which were intensified by CH_3^+ adsorbing, beneficial to the formation of the high-efficiency asymmetric ethanol.

¹ Shanghai Synchrotron Radiation Facility, Zhangjiang Laboratory, Shanghai Advanced Research Institute, Chinese Academy of Sciences, Shanghai 201204, China. ² Beijing Key Laboratory of Construction Tailorable Advanced Functional Materials and Green Applications, School of Materials Science and Engineering, Beijing Institute of Technology, Beijing 100081, China. ³ Department of Chemistry, Tsinghua University, Beijing 100084, China. ⁴ Shanghai Institute of Applied Physics, Chinese Academy of Sciences, Shanghai 201800, China. ⁵ National Synchrotron Radiation Laboratory, University of Science and Technology of China, Hefei, Anhui 230029, China. ⁶ School of Physical Science and Technology, ShanghaiTech University, Shanghai 201210, China. ⁷ These authors contributed equally: Xiaozhi Su, Zhuoli Jiang, Jing Zhou. ✉email: wxchen@bit.edu.cn; wangyu@sinap.ac.cn

Electrochemical conversion of carbon dioxide into value-added products using sustainable energies is environmentally friendly and economical approach¹. As well known, C₂₊ hydrocarbons or oxygenated compounds such as ethanol (C₂H₅OH), ethylene (C₂H₄) and n-propanol (n-C₃H₇OH) with remarkable energy densities have more value for solving the energy crisis². However, complex product selectivity limits the development and application of carbon dioxide reduction. The origin of this selectivity toward C₂₊ hydrocarbons has been a prominent topic of study recently and has been intensely debated^{3–6}. Copper-based materials are absolutely effective and promising catalysts for the reduction of carbon dioxide to multi-carbon products³. Previous works indicated that both the catalysts and substrates could affect the local structure and the electronic state of active sites, and then modify the reaction pathway and catalytic mechanism^{4,5}. Many strategies have been developed to modify or optimize the copper-based catalysts for improving the multi-carbon products selectivity, such as adjusting the surface morphology^{4,5,7–13}, doping metals or non-metals^{14–18}, building nanostructures^{19–21}, or designing single active sites^{22–25}.

Despite tremendous effort has been paid, further advances are still needed to understand the structure-activity relationship (SAR) and efficient conversion CO₂ to multi-carbon products especially for high economy asymmetric C₂₊ products (e.g., ethanol). Therefore, the design of catalysts that selectively produce ethanol via electrochemical CO₂RR were supposed to focus on minimizing three competing reaction pathways which reduced the faradaic efficiency (FE) of asymmetric ethanol by consuming electrons and protons, the hydrogen evolution reaction (HER), C₁ product formation (e.g., CH₄, HCOOH) and other symmetrical C₂ product formation (e.g., ethylene). However, little is known about the structure-activity relationship, extraordinarily to explain the catalyst structure changes with the product changes under different potential. Hence, it is urgent to build the structure-activity relationship between atomic structure and products for designing electrocatalysts.

Here we synthesized CuO clusters supported on nitrogen-doped carbon nanosheets (Cu/N_{0.14}C) as dispersed electrocatalysts, achieving high-performances CO₂ reduction that are superior to CuO_x catalysts in terms of stability, activity and selectivity. The prepared Cu/N_{0.14}C catalyst with appropriate nitrogen content displayed high C₂₊ products Faradaic efficiency of 73% which includes ethanol FE of 51% at the potential of –1.1 V vs. RHE with a current density of –14.4 mA/cm^{–2} in 0.1 M KHCO₃ electrolyte. Moreover, it exhibited superb long-term CO₂ electroreduction durability over 10 h. The well-defined self-reconstruction for the active sites of Cu/N_{0.14}C also facilitate the in-depth mechanistic understandings from complementary *Operando* Spectroscopy (XAS, XPS and FTIR), XANES simulations and theoretical calculations to present the atomic structure-activity relationship between the ethanol selectivity and in situ dynamic structure (local structure, electronic structure and the adsorbed intermediates), that would benefit the recognition for the CO₂RR process.

Results and discussion

Structure characterization of the Cu/N_xC. In a typical procedure, copper phthalocyanine and dicyandiamide were continuously mixed in ethanol and dried. Subsequently, the dried mixture was pyrolyzed at different temperatures for a series of Cu/N_xC samples with different nitrogen content (x = 0.14, 0.11, 0.02, 0, x is mass contents ratio of nitrogen to carbon). The linear sweep voltammetry (LSV) curves demonstrated that the activity of Cu/N_{0.14}C was better than other contrast samples with maximum current density. Transmission electron microscopy (TEM)

revealed that Cu/N_xC displayed a nano flake structure without obvious large-scale particles on the surface (Fig. 1a and Supplementary Fig. 1). The nanosheet structure was further confirmed by atomic force microscopy (AFM), and the corresponding height profiles of the scans showed a thickness of about 0.6 nm (Supplementary Fig. 2). The N species in the samples could prevent Cu atoms from aggregating excessively and ensured the atomic dispersion of Cu species. As we found in Supplementary Fig. 3, Cu nanoparticles (about 2–3 nano) were observed in the sample Cu/C (without N). High angle annular dark-field scanning transmission electron microscopy (HAADF-STEM), which can be clearly observed in the atomic phase, revealed that the copper atoms of Cu/N_{0.14}C agglomerate into clusters without an obvious lattice (Fig. 1b). Elemental mapping by Energy Dispersive Spectrometer (EDS) (Fig. 1c) demonstrates that nitrogen is uniformly dispersed within the carbon matrix. X-ray diffraction (XRD) revealed only a broad peak from the (002) of the Cu/N_{0.14}C and N_{0.14}C (Fig. 1d), however the Cu/C showed totally different peaks which could belong to a pure metallic copper (PDF#04-0836). The electron diffraction pattern of Cu/N_{0.14}C revealed it was amorphous material in Supplementary Fig. 4. To further study the electronic structure of the catalysis, Cu K-edge X-ray absorption spectroscopy, X-ray photoelectron spectroscopy (XPS) and soft-X-ray absorption spectroscopy (XAS) were carried out as shown in Fig. 1e–g and i and Supplementary Fig. 5. The Cu 2p_{3/2} XPS fitting curves revealed that Cu was mainly +1 and +2 valence in Cu/N_{0.14}C^{26,27}. The Cu L3M45M45 Auger electron spectroscopy (AES) showed no distinct peak around 918.5 eV which indicated that no Cu⁰ existed on the surface. The N K-edge presented four obvious resonances (Fig. 1i) assigned peak A₁, A₂, and A₃ to pyridine-like, cyanide-like, and graphite-like N, respectively, whereas A₄ at ~407 eV is attributed to the transition from N 1s core states to N–C σ* bonds²⁸. Obviously, peak A₃ of Cu/N_{0.14}C shifts negative energy which indicated the charge transfer had occurred compared with that of N_{0.14}C while other peaks keep the same position, indicating graphite-N formed a chemical bond with Cu sites²⁹. The C K-edge XAS spectra in Supplementary Fig. 5 showed no difference between Cu/N_{0.14}C and N_{0.14}C, excluding formation of the Cu–C bond. Thus, we could conclude that Cu sites only bond to graphite-like N, in Cu/N_{0.14}C.

X-ray absorption spectroscopy (XAS) measurements were employed to further investigate the electronic structure and geometric structure of the Cu/N_{0.14}C. Fig. 1e showed the Cu K-edge XANES spectra of the Cu/N_{0.14}C together with the references of CuO, Cu₂O and Cu foil. The absorption edge of the Cu/N_{0.14}C was between the Cu₂O and CuO, indicating that the oxidation state of the copper species is in the intermediate valence state between +1 and +2. The feature of XANES at 8986 eV and 8997 eV for Cu/N_{0.14}C resembled the mixture dominated by CuO with a little contribution by Cu⁺ or Cu⁰ complex. The Fourier-transformed (FT) k³-weighted EXAFS oscillation in Fig. 1f also showed the disappearance of the feature for Cu–Cu in R space in Cu/N_{0.14}C with simultaneous appearance of the peak at 1.5 Å for Cu–O/N. The fitting result displayed that the Cu–O/N bond length is 1.93 Å with the coordination number (CN) 3.4, (Supplementary Figs. 6, 7 and Table 1) indicating that Cu ions in the as-synthesized catalysts were predominately in the form of CuO clusters coordinated with four oxygen atoms. Notably, the coordination number of Cu–O/N is lower than that of the CuO (CN = 4) with a little shorter bond length (1.93 Å) (the bond length in CuO is 1.95 Å) suggesting that Cu species with a definite Cu–O/N coordination-unsaturated structure (CN < 4, bond length < 1.95 Å) existed. Note that TEM and EDX results showed CuO clusters were uniformly dispersed and anchored on the N-doped carbon nanosheets support. To further explore the N-doped that influenced CO₂RR activity, XANES and FT-EXAFS

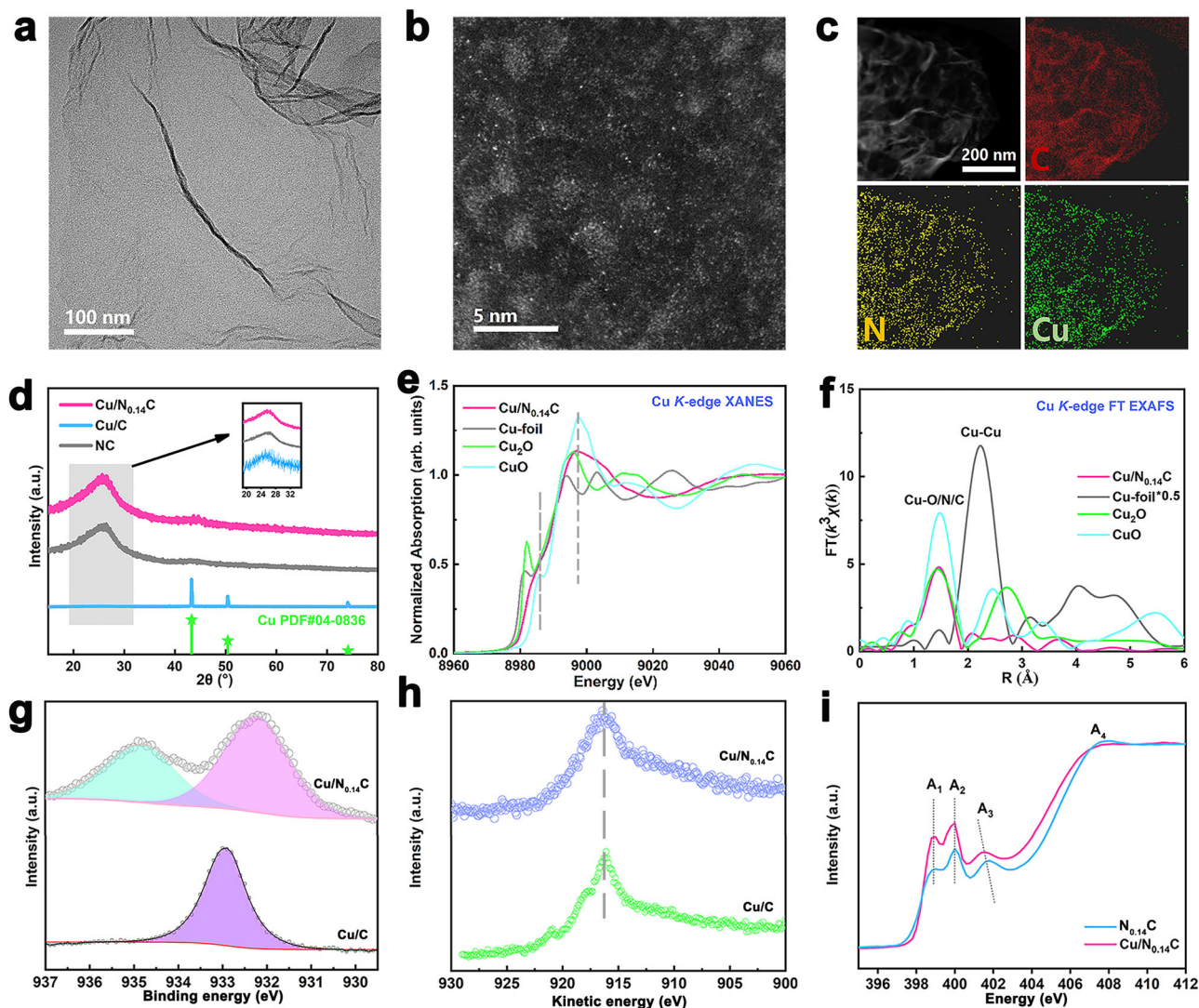


Fig. 1 Structure characterizations of the Cu/N_{0.14}C. **a** TEM image of Cu/N_{0.14}C. **b** HAADF-STEM image of Cu/N_{0.14}C. **c** EDS of Cu/N_{0.14}C. **d** XRD of Cu/N_{0.14}C, Cu/C and NC. **e** Cu K-edge XANES spectra of Cu/N_{0.14}C with the references. **f** FT-EXAFS spectra of Cu/N_{0.14}C with the references. **g** XPS analysis of the Cu 2p_{3/2} for Cu/N_{0.14}C and Cu/C. **h** AES analysis of the Cu L3M45M45 for Cu/N_{0.14}C and Cu/C. **i** N K-edge XANES spectra of Cu/N_{0.14}C and N_{0.14}C.

of Cu/C without the N-doping was plot in Supplementary Fig. 8. The XANES of the Cu/C indicated that the Cu ions were reduced to metallic Cu. The FT-EXAFS data also showed the peak for Cu–Cu in R space with the weak peak at 1.5 Å for Cu–O revealing that the copper in Cu/C agglomerated into larger metallic particles with a copper oxides surface in the air (more detail in Supplementary Figs. 9, 10 and Table 2). Our study indicated that N-doped promotes the dispersion of CuO clusters in the as-synthesized catalysts and played the critical role in improving FE for direct CO₂-to-ethanol electrochemical conversion. These results agreed well with XRD and HAADF-STEM results. The structure of the Cu/N_{0.14}C is further discussed by *operando* XAS.

Electrochemical characterization. The electrochemical CO₂RR activity of Cu/N_xC catalysts were evaluated in CO₂-saturated 0.1 M KHCO₃ solution. Linear sweep voltammetry (LSV) curves (Fig. 2a) demonstrated that the activity of Cu/N_{0.14}C was better than other contrast samples with lowest onset potential and maximum current density. This suggested that the increase in nitrogen content is helpful but limited to improve the activity.

Versus Cu/N_{0.14}C catalysts, the NC catalyst has little activity. Fig. 2b showed the product selectivity of CO₂RR of Cu/N_{0.14}C catalyst. The main products formed at low potential were CO and H₂. At –0.7 V (versus the reversible hydrogen electrode, RHE), hydrocarbons such as ethylene (C₂H₄) and methane (CH₄) started to form, and the selectivity of CO and H₂ decreased. The product of ethanol (C₂H₅OH) was first detected at –0.8 V vs. RHE. Subsequently, the faradaic efficiency (FE) of C₂₊ products continuously increased in the range –0.8 V to –1.1 V. At –1.1 V, the maximum FE of ethanol is 51% with a current density of –14.4 mA/cm² and the total C₂₊ products FE is up to 73%. We also gave the each product partial current density of Cu/N_{0.14}C catalyst in Fig. 2c. The LSV curves of Cu/N_{0.14}C in N₂ and CO₂ were measured, respectively, in Fig. 2d. In CO₂-saturated 0.1 M KHCO₃ solution, the Cu/N_{0.14}C displayed high activity. Fig. 2e showed that H₂, C₁ and C₂₊ products distributions of five catalysts. Cu/N_xC catalysts truly boosted the product selectivity of CO₂RR. We further evaluated the stability of Cu/N_{0.14}C for CO₂RR by a long-term experiment of 10 h. Both the partial current density and FE of C₂₊ products lightly decreased (Fig. 2f),

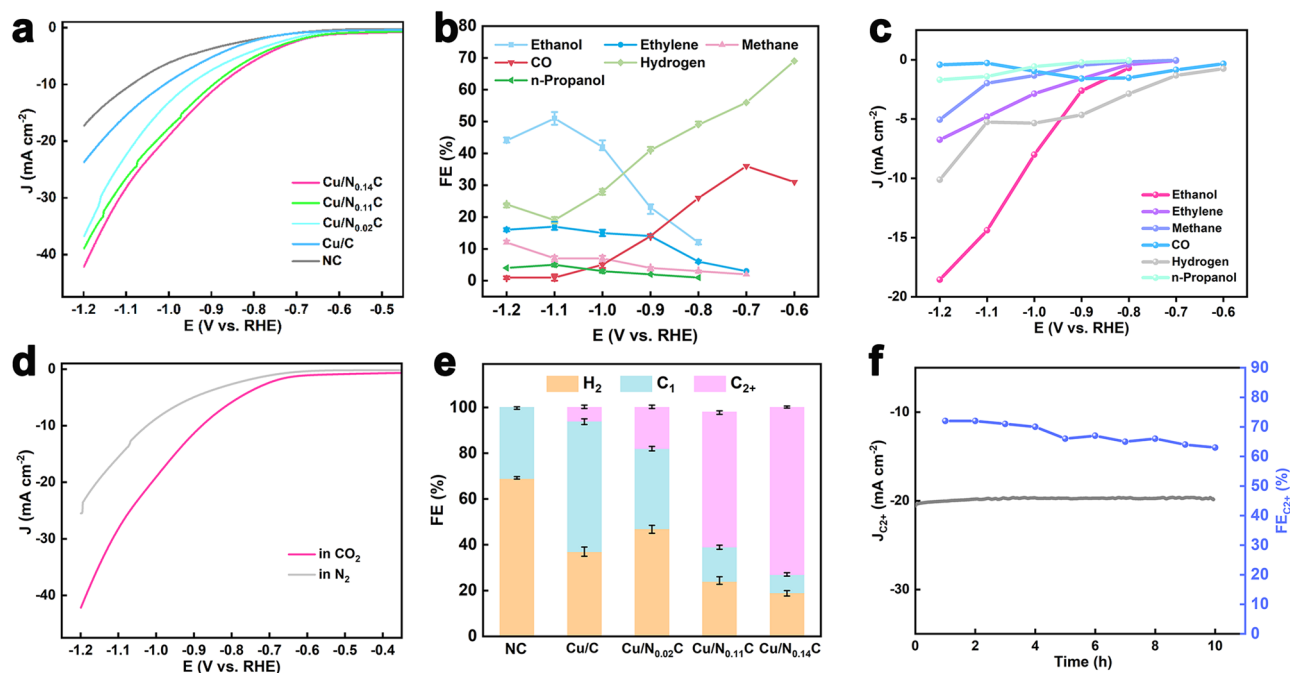


Fig. 2 CO₂RR activity of Cu/N_xC. **a** LSV curves of N_{0.14}C and Cu/N_xC. **b** FE and **c** Partial current density of each product of Cu/N_{0.14}C. **d** LSV curves of Cu/N_{0.14}C in N₂ and CO₂. **e** FE of H₂, C₁ and C₂₊ products of N_{0.14}C and Cu/N_xC. **f** Long-time stability of Cu/N_{0.14}C.

that demonstrated good stability. There were no structural changes of Cu/N_{0.14}C after long-term CO₂RR electrolysis, as shown in Supplementary Fig. 11.

Operando XAS, SR-FTIR Spectroscopy and Quasi-in-situ XPS-AES results. Studying the atomic structure-activity relationship of CO₂RR catalyst under *operando* conditions is crucial to reveal the intrinsic reactive mechanism. In order to identify the realistic catalytic centers of Cu/N_{0.14}C, *operando* XAS study were employed to directly monitor its catalytic behavior. We first collected ex-situ XAS data of the fully activated Cu/N_{0.14}C. When Cu/N_{0.14}C was soaked into the KHCO₃ solution at open circuit (OC), no obvious structural change was observed from the XANES in Supplementary Fig. 12. *Operando* XAS spectra recorded approximately every 10 min. There were drastic changes taking place in the sample at the very beginning when the potential was altered. Every spectrum was measured twice after the potential was kept constant for 30 min. XANES and derivative of XANES spectra under the altered potential were plotted in Fig. 3a and Supplementary Fig. 13. The oxidation state of Cu was estimated by comparing the energy position of the absorption edge. It could be clearly seen that XANES dramatically changed with the decreased applied potential indicating that this was a potential-dependent process. The gradual shift of the absorption edge to low energy side revealed a fall of the Cu valence state. An obvious critical potential at -0.8 V vs. RHE could be identified. The valence state of copper remained between $+1.0$ and $+2.0$ above this potential. Notably, there was a crude transfer to $+1.0$ at this critical potential. Below -0.8 V vs. RHE, Cu ions gradually get more deoxidized. Especially, the position of absorption edge was in the middle of Cu foil and Cu₂O when the potential was below -1.1 V, illustrating that the copper ions were nearly in averaged valence state of about $+0.5$. The changes of the atomic local structure around copper ions during CO₂RR were captured by FT-EXAFS, as shown in Fig. 3b. Wavelet transforms for the k^3 -weighted Cu *K*-edge EXAFS signals at OC, -1.1 and -1.4 V vs. RHE were plot in Fig. 3c. Under open-circuit condition,

FT-EXAFS data showed only one peak located at ~ 1.5 Å which is the typical scattering feature of Cu–N/O coordination. The FT EXAFS fitting results in Supplementary Figs. 5, 6 and Table 1 showed that CN of O/N atoms to Cu atoms was about 3.4 with an average bond length of 1.93 Å, without the Cu–Cu bond contribution. The Cu–O/N bond intensity slight decreased at -0.6 V vs. RHE. No C₂₊ products are formed at this stage in Fig. 2c. Once applying the potential of -0.8 V vs. RHE, the intensity of the scattering peak extremely descended with an additional peak at ~ 2.4 Å. This is a typical scattering feature of the Cu–Cu bond. The conversion of CO₂-to-ethanol reaction occurred concurrently. The intensity of Cu–O/N scattering peak further descended with the increasing of the Cu–Cu bond as the potential decreased. Moreover, the Cu–O/N peak intensity stabilized and the Cu–Cu bond slowly increased with the potential further decreasing to -1.1 V vs. RHE. The FT EXAFS fitting results (Fig. 3d, Supplementary Figs. 5, 6 and Table 1) indicated that the coordination number of the first Cu–O/N shell gradually decreased from 3.4 to 2.0 along with decreasing potential from OC to -1.4 V vs. RHE. In addition, the average Cu–O/N bond length slightly decreased. The coordination number of the Cu–Cu bond increased to 2.7 with a bond length of 2.53 Å, slightly shorter than that in Cu foil. The FT-EXAFS analyses are in agreement with the XANES data. Note that at -1.1 V vs. RHE with the maximum FE of ethanol, the metallic Cu–Cu coordination number was 2.0 and the CN of the Cu–O/N dropped down to 2.3 concurrently.

The transformation from CuO_x to Cu⁰ studied by *operando* XAS during electrochemical CO₂RR have been widely reported^{30–32}. However, Cu–Cu coordination number, extracted from EXAFS data fitting was usually larger than 8 with the disappearance of Cu–O bond, indicating that Cu nanoparticles formed with average sizes more than 1 nm³³. In this work, *operando* XANES spectra revealed that Cu/N_{0.14}C would not transfer to Cu⁰ totally and FT-EXAFS spectra showed Cu–N/O bond becoming steady with CN of 2.0. The stability of Cu–N coordination has been proved during electrochemical CO₂RR³⁴. These results suggested CuO clusters have almost reduced,

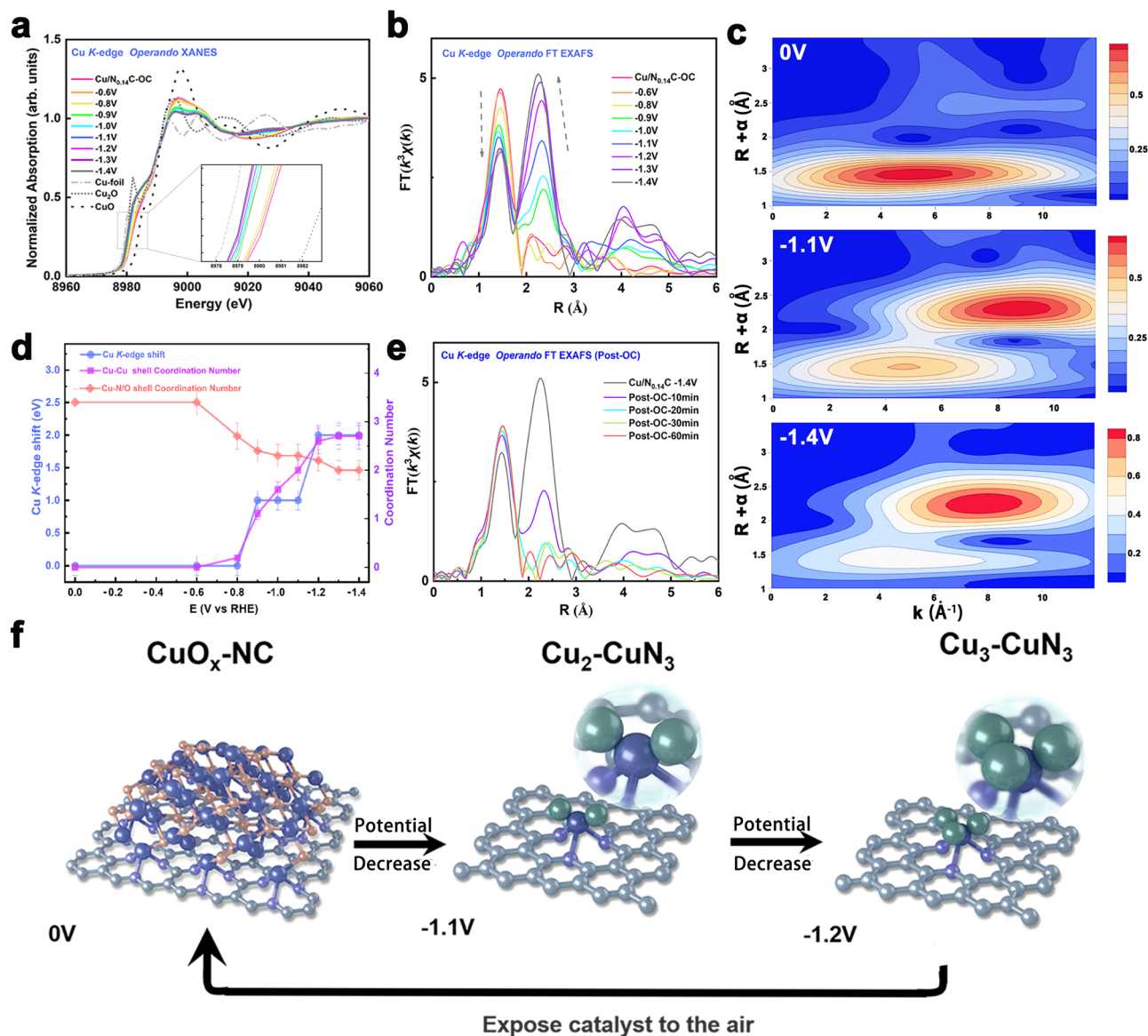


Fig. 3 Operando XAFS characterization of Cu/N_{0.14}C. **a** Cu K-edge operando XANES of Cu/N_{0.14}C from OC to -1.4 V vs. RHE in 0.1 M KHCO₃. **b** Operando FT-EXAFS of Cu/N_{0.14}C. **c** Wavelet transforms for the k^2 -weighted Cu K-edge EXAFS signals at OC, -1.1 V and -1.4 V vs. RHE during the CO₂RR. **d** The relationship of Cu/N_{0.14}C absorption edge, CN of first shell, CN of second shell and the potential. **e** Operando FT-EXAFS of Cu/N_{0.14}C after the applied potential was switched off and other conditions remained unchanged. **f** Proposed scheme for the reversible formation of the catalytically active Cu_n-CuN₃ cluster based on operando XAS and Quasi-in-situ XPS analysis (rufous, O; gray, C; purple, N; blue, Cu bond to both N and Cu; green, Cu just bond to Cu). All potentials are normalized to RHE.

leaving only Cu–N bond of the CuN_x. XAFS is the technique measuring average values over all Cu species. Therefore, the fitting coordination number of Cu–N (CN = 2.0 at -1.4 V vs. RHE) was lower than the coordination number of the true active sites since a large part of Cu atoms bond to another Cu atoms (Cu–Cu CN > 2). On the other hand, considering that a definite Cu–N coordination-unsaturated structure (CN < 4) existed in Cu/N_{0.14}C, we suggested that Cu–N CN of the remaining CuN_x is 3, $x = 3$. Moreover, EXAFS fitting results also indicated the Cu coordination shell switched from Cu–O to Cu–Cu with an unusual low coordination number of 2.0 at -1.1 V vs. RHE, with the maximum FE of ethanol. There are two possible structures of the in situ generated Cu species of Cu/N_{0.14}C, according with the Cu–Cu CN of 2.0. One is that the formation of ultrasmall Cu moiety, Cu_n, where $n = 3$ ³⁵, while the other one is a mixture of CuN₃ sites and Cu metal particles.

We further integrated two evidence to prove the formation of the Cu₃ moiety rather than metal particles. Firstly, we found that the potential-dependent transformation was reversible and in situ generated Cu species were highly unstable and could be easily oxidized in the absence of the applied potential. As shown in Fig. 3e and Supplementary Fig. 14, an operando XAS was performed on this sample after the applied potential was switched off and other conditions remained unchanged. It could be obviously seen that Cu–O/N bond increased, with Cu–Cu bond disappeared concurrently, indicating that the coordination environment reversed from Cu–Cu shell to Cu–O/N shell. Notably, the Cu–O/N bond was still lower than that of the initial fully activated sample. At last, the KHCO₃ solution was poured out and the catalyst was in air atmosphere, and ex-situ XAS was performed on this sample. Its spectral shape was identical to that of the initial fully activated sample, as shown in Supplementary

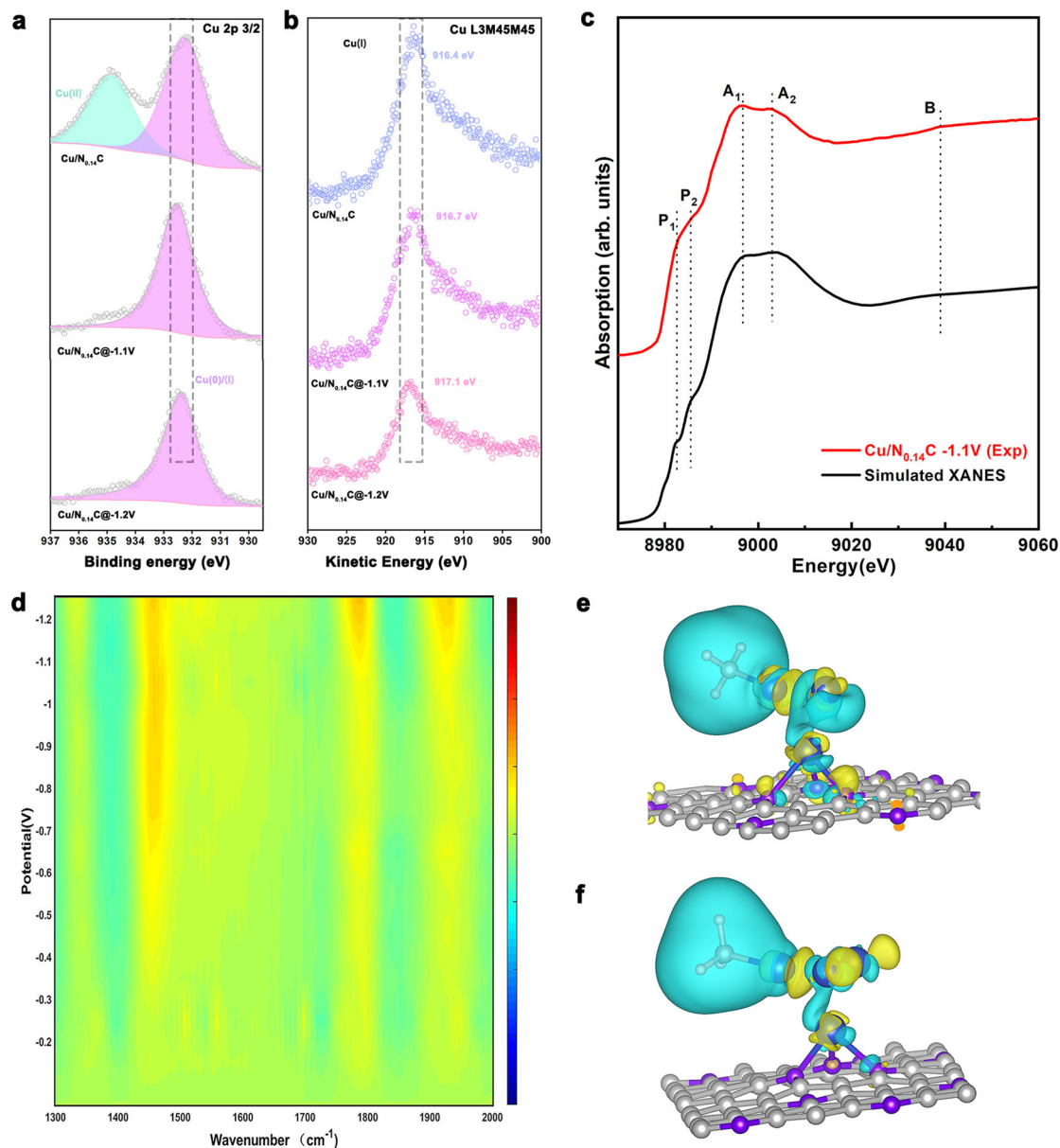


Fig. 4 Complementary Operando spectra characterizations, XANES simulation and DFT calculations. **a** Quasi-in-situ XPS of the Cu 2p 3/2 for Cu/N_{0.14}C. **b** Quasi-in-situ AES of the Cu L3M45M45 for Cu/N_{0.14}C. **c** Comparison between the Cu K-edge XANES experimental spectra (red line) and the theoretical spectra (black line) calculated with the Cu₂-CuN₃ cluster. **d** Operando SR-FTIR of Cu/N_{0.14}C. Electron density difference plot of the **e** Cu₂-CuN₃ cluster, **f** Cu₃-CuN₃ cluster. Blue and yellow represented the electron accumulation and deletion, respectively. The balls in gray, purple, blue and white represented C, N, Cu, and H atoms, respectively. All potentials were normalized to RHE.

Fig. 15, suggesting the Cu species remained to be oxidized and dispersed in the air. This result agreed well with HAADF-STEM results after CO₂RR electrolysis in Supplementary Fig. 11. The conversion process of the Cu/N_{0.14}C catalyst was shown in Fig. 3f. On the other hand, we performed *operando* XAS on the Cu/C in Supplementary Fig. 16. The XANES and FT-EXAFS of Cu/C were mostly unchanged, verifying the Cu metal particles were very stable and could not be easily oxidized. Therefore, we could rule out the existence of Cu metal particles possibility.

Secondly, we carried out Quasi-in situ x-ray photoelectron spectroscopy (XPS) and Auger electron spectroscopy (AES) analysis to prove the valence of Cu species of Cu/N_{0.14}C remain at +1 without Cu⁰ under the altered potential. The Quasi-in situ XPS and AES results were shown in Fig. 4a, b. The Cu/N_{0.14}C showed two peaks at 934.6 eV and 932.2 eV, which corresponded

to Cu²⁺ and Cu⁺/Cu⁰ 26,27. The peak at 934.6 eV disappeared at the -1.1 V vs. RHE, which indicated the Cu²⁺ was reduced during the CO₂RR process. The peaks around 932 eV still remained. To verify the valence of the Cu, AES was employed to distinguish Cu⁺/Cu⁰ species. The peaks around 916.5 eV showed a little shift indicating that the sample would retain the valence at +1 during the CO₂RR process^{36,37}. The XPS detected the valence state information with depth sensitivity of 1–10 nm³⁸. Therefore, there are no Cu metal particles existing under the electrochemical conditions. Notably, the Cu AES shifted to the higher kinetic energy with the potential reduced, indicating fewer electrons on average Cu were transferred to the nitrogen-doped carbon support of the -1.2 V vs. RHE. The catalysis electron configuration would obviously affect the adsorption of the non-polar molecule, which played an important role during the reduction process^{39,40}.

Probably, the ethanol productivity declined at -1.2 V vs. RHE, because the larger cluster could lead to the Cu^0 electron configuration increasing^{32,41}. Interestingly, the Quasi-in situ XPS of the Cu/C showed different changes during the CO_2 RR process, as shown in Supplementary Fig. 17. The binding energy of the Cu $2p_{3/2}$ peak for the pristine Cu/C was at 932.9 eV and the kinetic energy L3M45M45 peaks located at 916.4 eV correspond to the Cu^+ species^{37,42}, which may be due to the surface oxidation during exposing to air. The XPS altered completely after CO_2 RR process at -1.1 V vs. RHE. The binding energy of Cu $2p_{3/2}$ peak located at 932.7 eV and the kinetic energy L3M45M45 peak located at 918.5 eV corresponding to Cu^0 ^{36,43}, indicating that catalysts would not be oxidized in the transfer process. Therefore, the Cu/C without N-doping had a Cu^0 electron configuration with high H_2 productivity and less multi-carbon productivity. These data agreed well with the XAFS results, identifying a strong relationship between the structure of the catalysis and selectivity of multi-carbon products formation.

Hence, we can consequently conclude that the Cu–Cu bond of the *operando* spectroscopy was from in-situ generated ultrasmall Cu moieties, Cu_n , under the electrochemical conditions, where $n = 3$ at -1.1 V vs. RHE. Three Cu atoms chemically bonded to each other with the Cu–Cu coordination number of 2 and one Cu atom bonded to three graphite-like N, forming the $\text{Cu}_2\text{–CuN}_3$ moiety, as shown in Fig. 3f. Such Cu_3 moieties which are similar to copper clusters⁴⁴ have geometric shapes of equilateral triangles, and anchored on the N-doped carbon nanosheets support. The Cu–N bonds play an important role to disperse and anchored the Cu_3 moiety uniformly. Moreover, the coordination number of Cu–Cu increased to 2.6 with the potential decreased to -1.2 V vs. RHE, suggesting the Cu_4 appeared with tetrahedron configuration of the $\text{Cu}_3\text{–CuN}_3$ moiety and the ethanol productivity declined accordingly. Notably, the in-situ generated $\text{Cu}_n\text{–CuN}_3$ cluster can't exist without the applied potential. Furthermore, one CH_3^* was adsorbed to one Cu atom according to *operando* FTIRS results in the next discussion. Therefore, there are the other two oxygen atoms which were adsorbed to another Cu atom, because of the average Cu–N/O coordination number ~ 2 . The cluster was shown in Supplementary Fig. 18. The theoretical XANES spectrum was also calculated to confirm that it was the active site based on convolution results for every considered model around each Cu atom. It could be found that the simulated result for this model could reproduce the main features of the experimental XANES at -1.1 V vs. RHE well in Fig. 4c. Two oxygen atoms may be from the adsorbed groups, such as OH^* , OCHO^* (or CO_2), as shown in Supplementary Fig. 19a, c. The experimental spectra were both properly reproduced in Supplementary Fig. 19b, d. The simulated spectra were similar to the spectrum that was calculated without the adsorbed groups. A slight change in the structure of the 2nd shell does not significantly affect the simulated XAFS spectrum, especially for the H atom. On the other hand, the XANES spectra of the references with different local structures were used to compare with XANES of the $\text{Cu/N}_{0.14}\text{C}$ at -1.1 V vs. RHE and rule out Cu– N_2 site, Cu– N_3 site with trigonal planar geometry, Cu– N_4 sites (including tetrahedral geometry, square planar geometry and Cu– N_3 with CH_3^*) and different sizes Cu nanoparticles as shown in Supplementary Figs. 20–23. We also tried linear combination fitting (LCF) of XANES of Cu NPs with different sizes and various Cu– N_4 sites, as shown in Supplementary Fig. 24. We could not obtain a fitting spectrum which was matched with *operando* XANES at -1.1 V vs. RHE. The main features of LCF result were notable different from that of *operando* XANES. Therefore, the possibility of combining for Cu NPs with different sizes and various Cu– N_4 sites could be excluded.

In order to verify that $\text{Cu}_2\text{–CuN}_3$ clusters in-situ generated are truly metastable catalyst and the potential-dependent reversibility was real chemical reaction, the freeze-quench approach was used to freeze the redox state and local structure of the catalyst and measured XAFS data at liquid helium temperatures (18 K), as shown in Supplementary Fig. 25a. The X-ray edge energy as well as the spectral shape of the freeze-quench and *operando* spectra do not differ significantly in Supplementary Fig. 25b–d. This comparison verified that the freeze-quench and *operando* method access the same electrochemical state of the $\text{Cu/N}_{0.14}\text{C}$ (same oxidation state and local structure). The spectra which were measured for three times could be perfectly overlapped in Supplementary Fig. 25e–g. These results indicated that $\text{Cu}_2\text{–CuN}_3$ clusters oxidized without the applied potential was the chemical reaction and $\text{Cu}_2\text{–CuN}_3$ clusters in-situ generated material were truly metastable catalysts.

Overall, *Operando* XAS study revealed that a transformation from $\text{Cu/N}_{0.14}\text{C}$ to unique ultrasmall Cu_n moiety and presented the structure-activity relationships of this catalyst, indicating the in-situ generated $\text{Cu}_2\text{–CuN}_3$ cluster is the optimal site for CO_2 reduction to ethanol.

To further reveal the key adsorbed intermediates in the catalytic reaction, we carried out Synchrotron radiation *operando* Fourier-transform infrared spectroscopy (SR-FTIRS). No obvious absorption band was observed on scanning the applied potential ranging from -0.1 V to -0.7 V vs. RHE (Fig. 4d). Interestingly, distinct vibration features were observed at 1450 cm^{-1} when applied potentials were lower than -0.7 V vs. RHE, which could be assigned to the antisymmetric methyl groups vibration of CH_3^* ^{45,46}, an important intermediate for C_2 formation rates. Furthermore, when the applied potential was below -1.1 V vs. RHE, two new bands at $\sim 1780\text{ cm}^{-1}$ and 1920 cm^{-1} could be ascribed to the surface-bound C=O species^{12,47} and electrogenerated CO bound to copper surface^{12,48} suggesting H^* radicals were consumed by other products at -1.2 V vs. RHE, which was consistent with the electrochemical results (Fig. 2c). The FE of the ethanol reached a high point at -1.1 V vs. RHE and then decreased obviously at lower potential to accompany the hydrogen rate increased. The FE of ethanol reversed at -1.2 V vs. RHE may be due to the Cu cluster enlarging that lead to the competing reaction of HER and CO_2 RR hydrogenation to CH_4 enhancing, which blocked the CO_2 to ethanol^{41,49}. These FTIRS analysis showed uniformity with *operando* XAS and XPS results. On the other hand, the infrared bands for CH_3^* over the Cu/C catalyst were not observed even after applying potential at -1.2 V vs. RHE in Supplementary Fig. 26. The intensities were much lower than those over the $\text{Cu/N}_{0.14}\text{C}$. These results were consistent with the low C_{2+} formation rates of the Cu/C catalyst, further confirming the unique structure of $\text{Cu/N}_{0.14}\text{C}$ under the electrochemical condition. Therefore, FTIR results provided experimental evidence for the conversion of CO_2 -to-ethanol reaction mechanism and demonstrated that CH_3^* was the major intermediates covered the catalysis. To further investigate the property of the adsorption species, the isotope labelling *operando* FTIR was measured under the reaction condition, as shown in Supplementary Fig. 27. With H_2O replaced by D_2O in the electrolyte, the peak shifted to 1190 cm^{-1} obviously indicating that it could be assigned to the vibration of hydrogen group (CD_3^*). This result was consistent with previous speculate. Therefore, the FTIR results suggested that the adsorption of CO_2 was the rate-determining step after CH_3^* formed. It may be highly affected by mass transfer process. The results are consistent with previous reports whereby the selectivity of C_{2+} products formation increased with the density of CO_2 ^{50,51}.

Density functional theory calculations. Theoretical investigations were conducted based on DFT calculations to further understand the reaction mechanism of the $\text{Cu}_2\text{-CuN}_3$ cluster with CH_3^* adsorbed. A supported $\text{Cu}_2\text{-CuN}_3$ cluster model with a Cu bonding with three N atoms on N-doped carbon nanosheets was proposed to be the structure of active sites with an applied potential of -1.1 V vs. RHE in Supplementary Fig. 28a. For comparison, we built a model of $\text{Cu}_3\text{-CuN}_3$ cluster in Supplementary Fig. 28b that represent for the growth of Cu clusters and may be the active site for the more negative applied potential. The calculated average partial charge of three copper atoms in the $\text{Cu}_2\text{-CuN}_3$ cluster was $+0.20\text{ e}^-$ because of the charge transfer between the cluster and N-doped carbon nanosheets. The charge exchange primarily occurred with the Cu atom bonding with N atoms. The other two Cu atoms changed slightly before the reaction occurred, which profited from the absorption of C atoms. This was similar to the $\text{Cu}_3\text{-CuN}_3$ cluster. The difference was that the average partial charge was $+0.15\text{ e}^-$. Interestingly, the charge distribution between Cu atoms was charge-asymmetry as shown in Fig. 4e f. The major charge transfer occurred at Cu-N₃ site. The N-doping played an important role to adjust the electron transfer and further charge distribution between the Cu atoms and N-doped carbon interface.

Theoretical investigations were conducted based on DFT calculations to further understand the reaction mechanism of the Cu-N₃ with triangle pyramid geometry, Cu-CuN₃, Cu₂-CuN₃, and Cu₃-CuN₃ in Supplementary Fig. 20c, f, g, h. The supported CuN₃, Cu-CuN₃, Cu₂-CuN₃ and Cu₃-CuN₃ models with a Cu bonding with three N atoms on N-doped carbon nanosheets which were proposed to be the structure of active sites with the applied potential and represents the growth of Cu clusters that may be the active site for the formation of ethanol according the results of *operando* XAS analysis. The reaction pathway of CO₂RR to CH₃CH₂OH for the Cu₂-CuN₃ cluster was investigated combined by the computational hydrogen electrode approach as shown in Fig. 5a, b, Supplementary Fig. 28, and Supplementary Data 1–13⁵². The $^*\text{OCHO}$ mechanism was preferred for our catalysts than the $^*\text{CO}$ mechanisms, due to the production of CO was suppressed along with the formation of ethanol at the potentials below -0.8 V as shown in Fig. 2b. CO₂ molecules interact with two exposed Cu atoms, respectively, forming coadsorbed ($^*\text{OCHO} + ^*\text{OCHO}$) (State 3). One adsorbed $^*\text{OCHO}$ was firstly reduced to form $^*\text{CH}_3 + ^*\text{OCHO}$ (State 9), and then the other $^*\text{OCHO}$ was reduced to construct $^*\text{CH}_3 + ^*\text{OCH}_2$ (State 12), that went through the C-C

bond formation to CH₃CH₂OH. Similar reaction processes based on $^*\text{OCHO}$ mechanism were considered for Cu₃-CuN₃, as well as CuN₃ and Cu-CuN₃ which contained only one active Cu site, as shown in Supplementary Fig. 29. The calculated overpotential (-0.501 V) for Cu₂-CuN₃ cluster was much lower than that of CuN₃ (-1.685 V), Cu-CuN₃ (-1.368 V) and Cu₃-CuN₃ (-0.699 V), implied that the Cu₂-CuN₃ observed by *operando* XAS is the real active site for reduction of CO₂ to ethanol, as shown in Supplementary Fig. 30. Furthermore, there were relatively high energy barriers for State 8 → 9 (-0.501 eV) and State 11 → 12 (-0.467 eV) in the reaction process of Cu₂-CuN₃, both of which containing $-\text{CH}_3$ and easy to be detected in accordance with our FTIR results.

The hydrogen evolution reaction is a competing reaction with CO₂RR^{53,54}. Therefore, the competing relationship between CO₂RR and HER should be considered. The adsorption energy was calculated to further investigate the difference between Cu₂-CuN₃ and Cu₃-CuN₃. The adsorption energy of H^{*} showed that the Cu₃-CuN₃ model (-0.36 eV) had a much lower energy than the Cu₂-CuN₃ model ($+0.15\text{ eV}$). The CO₂ adsorption energy for Cu₂-CuN₃ and Cu₃-CuN₃ has been calculated and the result shown that the adsorption energy of CO₂ for Cu₂-CuN₃ and Cu₃-CuN₃ are $+0.24\text{ eV}$ and $+0.18\text{ eV}$, respectively, implying the adsorption capacities for Cu₂-CuN₃ and Cu₃-CuN₃ are close. However, the corresponding adsorption energy is $+0.15\text{ eV}$ (Cu₂-CuN₃) and -0.36 eV (Cu₃-CuN₃), respectively, indicating the adsorption capacities of H for Cu₃-CuN₃ are much stronger than that for Cu₂-CuN₃. These results shown the adsorption processes of both CO₂ and H at the Cu₂-CuN₃ are non-spontaneous processes. On the contrary, for Cu₃-CuN₃, the adsorption of the H is spontaneous process, while the adsorption of CO₂ is still non-spontaneous process, illustrating the H adsorption is advantage state for the competing reaction. Therefore, the larger amounts of H were adsorbed on the Cu₃-CuN₃ sites, which preempted the adsorption sites of CO₂ and reduced the amount of ethanol produced. It corresponded with the competing reaction of H₂ and CH₄ increasing when the potential decreased.

CH₃^{*} was the key intermediate for C₂⁺ formation rates and it occurred when the potential decreased to -0.6 V vs. RHE. This result suggested the rate-determining steps (RDS) altered when the potential at decreased to -1.2 V vs. RHE, combining the FTIR results in Fig. 4d. To further analysis why RDS changed during the reaction, the different charge density for Cu₂-CuN₃ (with/without CH₃^{*}) and Cu₃-CuN₃ (with/without CH₃^{*}) was

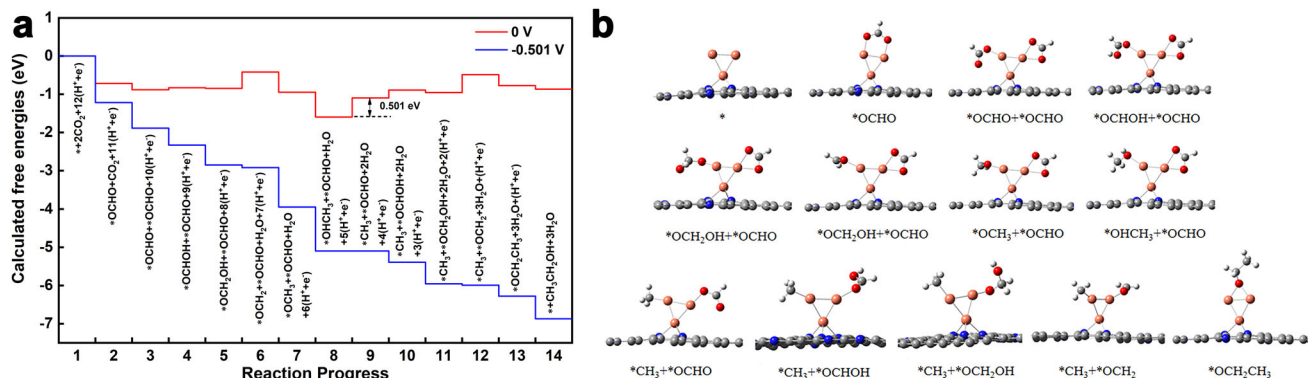


Fig. 5 DFT calculations of CO₂RR activity. **a** Reaction progress of CO₂ to CH₃CH₂OH on the Cu₂-CuN₃ at 0 V and -0.501 V applied potential. The * showed the reaction site. The state with the highest energy barrier (0.501 eV) is 8 → 9. All states involving the transfer of the ($\text{H}^+ + \text{e}^-$) pair were electrochemical reaction states, except for the 12 → 13 state ($\text{CH}_3^* + \text{OCH}_2^* \rightarrow \text{OCH}_2\text{CH}_3^*$), which was the C-C bond formation and not influenced by applied potential. **b** Local structures of the active site and intermediate state. The balls in brown, blue, red, gray and white represent Cu, N, O, C, and H atoms, respectively.

calculated as showing in the Fig. 4e, f and Supplementary Fig. 31. The charge density differential diagram indicated the nonbonding Cu atoms in the $\text{Cu}_2\text{-CuN}_3\text{-CH}_3$ got $0.15 e^-$ and the charge accumulation occurred. These results showed that charge-asymmetry effected intensified by CH_3^* adsorption. Due to the charge accumulation, a polarization electrical field was presented that could modulate the CO_2 reduction reaction and reduce the thermodynamic energy barrier for the reaction⁵⁵. The electron-rich Cu atoms enhanced the boundary oxygen sites of the adsorbed CO_2 , which protected the oxygen end from being protonated and occupied the valence electron of carbon to avoid the C=C double bond formation⁵⁶.

Conclusions. In summary, we systematically investigated a catalyst in which CuO clusters are supported on nitrogen-doped carbon nanosheets ($\text{Cu/N}_{0.14}\text{C}$) for efficient CO_2 electroreduction. The catalysts delivered high C_2^+ products FE (~73%), which included an ethanol FE of 51% at the potential of -1.1 V vs. RHE and the current density of -14.4 mA/cm^2 in 0.1 M KHCO_3 electrolyte. *Operando* XAS and XPS results revealed a potential-dependent structure transformation from CuO cluster to $\text{Cu}_n\text{-CuN}_3$ moiety, which is a reversible process. Once $\text{Cu}_2\text{-CuN}_3$ clusters have been formed at -1.1 V, CO_2 conversion to ethanol occurs with the maximum FE, indicating the $\text{Cu}_2\text{-CuN}_3$ cluster is the optimal site. The N-doping played an important role to disperse the reduced Cu_n cluster uniformly and adjust charge distribution between metal atoms and substrate. *Operando* FTIR and theoretic calculations results demonstrated that CH_3^* was the major intermediates and $\text{Cu}_2\text{-CuN}_3$ clusters were charge-asymmetric sites that are intensified by CH_3^* adsorbing. The charge-asymmetric sites are responsible for the outstanding asymmetry ethanol formation. Overall, our findings suggest a strategy engineering the pre-catalysts to modulate the electron transfer and in-situ generate ultrasmall metal clusters anchored on the substrate as high dispersion asymmetric sites, which is the key factor to facilitate the formation of asymmetric products. It would extend to the single-atomic site, oxide composite structure, and metal-support effect. These catalysts have great potential to exhibit novel catalytic properties such as more efficient catalytic performance and higher selectivity compared to the single atom catalysts and oxide catalysts.

Methods

Preparation of $\text{Cu/N}_x\text{C}$ and the comparison samples. Typically, 100 mg copper phthalocyanine and 1.0 g dicyandiamide were continuously mixed in ethanol and entirely dried. Subsequently, the dried mixture was pyrolyzed for 2 h in the N_2 atmosphere at different temperature to obtain a series of $\text{Cu/N}_x\text{C}$ samples with different nitrogen content ($x = 0.14, 0.11, 0.02$, corresponding pyrolysis temperature at 800 °C, 900 °C, 1000 °C, respectively. x is mass content ratio of nitrogen to carbon). Collect obtained black powder after pyrolysis and directly used for further characterizations and catalytic performance test. Cu/C was prepared with copper chloride and trimesic acid. The pyrolysis temperature was 800 °C and other synthesis conditions were the same as above.

Characterization. TEM images were carried out by the JEOL JEM-2100F microscope (200 kV). AFM was obtained on SPM-960 AFM. Typically, small amount of sample was ultrasonically dispersed in the aqueous solution. For AFM measurement, 10 μL of the completely dispersed solution was carefully dropped on a flat mica sheet, and then placed it in a fume hood to air dry. For TEM, 10 μL of the dispersed solution prepared above was dropped on a copper mesh with carbon support film. EDS elemental mapping and HAADF-STEM were characterized by a JEOL ARM-200 microscope (200 kV) with a probe spherical aberration corrector. X-ray powder diffraction (XRD) spectra were observed by RigakuTTR-III XRD of Cu $K\alpha$ radiation ($\lambda = 1.5418 \text{ \AA}$). XPS spectra were acquired on a PerkinElmer Physics PHI 5300 spectrometer⁵⁷.

Electrochemical measurements. Electrochemical measurements were accomplished in a gas-tight H-type cell at CHI 760E electrochemical workstation (Shanghai Chenhua, China). For preparation of the working electrode, 2 mg of the catalyst was dissolved in 500 μL solution (including 10 μL Nafion solution (5 wt %)

and deionized water/ethanol (volume ratio, 1:4)) to form a well-dispersed catalyst ink. Furthermore, we dropped 10 μL ink on the glassy carbon electrode. The catalyst loading is about 0.2 mg/cm^2 . The Ag/AgCl electrode and platinum plate were employed as the reference electrode and counter, respectively. The cathodic chamber and anodic chamber were separated by Nafion 117 membrane. All the potential was reported versus RHE. The conversion between different electrode potentials used the following formula: $E_{\text{RHE}} = E_{\text{Ag/AgCl}} + 0.197 \text{ V} + 0.0591 \times \text{pH}$. LSV (the scan rate of $10 \text{ mV}\cdot\text{s}^{-1}$) and CV experiments ($50 \text{ mV}\cdot\text{s}^{-1}$) were implemented to test the catalytic performance in CO_2 -saturated 0.1 M KHCO_3 electrolyte, respectively⁵⁷. Comparison of CO_2 RR activities for the other catalysts were shown in Supplementary Table 3.

Operando XAFS Measurements. The computer-controlled electrochemical analyzer was used to conduct electrochemical measurements. The catalyst modified carbon paper, Pt plate and Ag/AgCl (KCl-saturated) electrode were employed as the working electrode, counter electrode and reference electrode, respectively. The plexiglass electrochemical cell which had the flat wall with a circular hole of 15 mm diameter. was applied for *operando* XAFS measurements. $\text{Cu/N}_x\text{C}$ catalyst coated carbon paper contacted with the copper slip and the catalyst layer faced inward. Afterwards we poured KHCO_3 solution into the cell which was connected to the electrochemical station with the copper tape. The organic glass upper cover of the cell with the Ag/AgCl reference electrode was used to fix the distance between reference electrode and working electrode from start to finish⁵⁷. *Operando* XAFS data were measured with fluorescence mode using the Ar-filled Lytle detector.

Operando SR-FTIR Measurements. *Operando* SR-FTIR measurements were conducted at the infrared spectroscopy and microspectroscopy station (BL01B) of National Synchrotron Radiation Laboratory (NSRL) ⁵⁸. The CHI 660E electrochemical workstation (Shanghai Chenhua, China) was used to apply voltage to a self-made infrared reflection cell. The infrared spectrums were collected using Bruker Vertex 70 V/s FTIR spectrometer with nitrogen cooled mercury cadmium telluride detector, and the synchrotron radiation infrared beam was focused on the reflection cell using Bruker Hyperion 3000 microscope equipped with a $\times 15$ objective. In the measurements, the gap between the working electrode and the ZnSe window was carefully maintained on the order of microns to prevent excessive water absorption. All spectrums were collected using single-potential alteration FTIR spectroscopy and were acquired by averaging 128 times scan with a 4 cm^{-1} resolution, and the background spectrums was conducted under open-circuit voltage, the voltage ranges for conducting measurements were 0 V to -1.2 V with an interval of 0.1 V.

Quasi-in situ XPS and AES. Quasi-in situ X-ray photoelectron spectroscopy was conducted of catalysts drop-casted on carbon paper as same as mentioned in Electrodes section. Before test the electrolytes should be CO_2 -saturated to remove the dissolved oxygen in the solution. Samples were conditioned at different potential for 30 min as one conditioning step. After that the samples was moved to the XPS vacuum chamber without extra exposed to the air. That would avoid the air to influence the catalysts to keep the authentic state under the CO_2 RR process. XPS (ESCALAB 250X) was measured at Analytical Instrumentation Center, Shanghai Tech University. It was used to characterize the chemical bonding character of the obtained catalysts using a monochromatic of 1486.6 eV (Al $K\alpha$ source). All XPS spectra were corrected by C 1s peak with the binding energy at 284.6 eV. All of the reagents were used without further purification.

Freeze-quench XAS. The $\text{Cu/N}_{0.14}\text{C}$ was electrodeposited on a carbon paper electrode, which was an integral part of the XAS sample holder. The $\text{Cu/N}_{0.14}\text{C}$ was equilibrated potentiostatically for 20 min at -1.1 V vs. RHE. The $\text{Cu/N}_{0.14}\text{C}$ electrode was rapidly frozen by immersion in liquid nitrogen. The chemical reaction is extremely slow at low temperature environment and the chemical state of the catalyst was well preserved for XAFS data collection periods. X-ray absorption spectra at the Cu K-edge were collected at beamline BL14W1 of the SSRF using a Lytle detector with the Ni filter. The measurements were performed at 18 K using a cryostat (ARS). The excitation energies (scan range 8779–9779 eV) were selected by a Si (111) double-crystal monochromator.

Computational methods. DFT calculations were performed within the frame of plane-wave-based density functional theory (DFT) by VASP package. The generalized gradient approximation (GGA) in the Perdew–Burke–Ernzerhof (PBE) formalism was adopted to treat the electron exchange and correlation energy. The cut-off energy was set to be 500 eV. For structural optimization, $3 \times 3 \times 2$ k-points meshes with a the original Monkhorst-Pack scheme was used and the convergence of energy and force were 10^{-6} eV and 0.01 eV \AA^{-1} , respectively. $6 \times 6 \times 4$ k-points meshes were used for static calculations. A 20 Å vacuum layer in the z-axis direction was added to avoid the interfere of the layer image coupling caused by the periodic boundary conditions⁵⁹. For more details, please see Supplementary Figs. 20, 28, 29, 31 and Supplementary Data file 1–13.

Data availability

The data supporting the findings of this work are available within the article and its Supplementary Information files. The DFT data for cluster and reaction pathway as cif files are provided as a Supplementary Data file 1–13. All the data reported in this work are available from the authors on reasonable request. Source data are provided with this paper.

Received: 10 November 2020; Accepted: 23 February 2022;

Published online: 11 March 2022

References

- Zhang, W. et al. Progress and perspective of electrocatalytic CO₂ reduction for renewable carbonaceous fuels and chemicals. *Adv. Sci.* **5**, 1700275 (2018).
- Zheng, Y. et al. Understanding the roadmap for electrochemical reduction of CO₂ to multi-carbon oxygenates and hydrocarbons on copper-based catalysts. *J. Am. Chem. Soc.* **141**, 7646–7659 (2019).
- Popovic, S. et al. Stability and degradation mechanisms of copper-based catalysts for electrochemical CO₂ reduction. *Angew. Chem. Int. Ed.* **59**, 14736–14746 (2020).
- Yang, K. D. et al. Morphology-directed selective production of ethylene or ethane from CO₂ on a Cu mesopore electrode. *Angew. Chem. Int. Ed.* **56**, 796–800 (2017).
- Kim, D., Kley, C. S., Li, Y. & Yang, P. Copper nanoparticle ensembles for selective electroreduction of CO₂ to C₂–C₃ products. *Proc. Natl Acad. Sci. USA* **114**, 10560–10565 (2017).
- Chatterjee, T., Boutin, E. & Robert, M. Manifesto for the routine use of NMR for the liquid product analysis of aqueous CO₂ reduction: from comprehensive chemical shift data to formaldehyde quantification in water. *Dalton T.* **49**, 4257–4265 (2020).
- Resasco, J. et al. Promoter effects of alkali metal cations on the electrochemical reduction of carbon dioxide. *J. Am. Chem. Soc.* **139**, 11277–11287 (2017).
- Schouten, K. J., Qin, Z., Perez Gallent, E. & Koper, M. T. Two pathways for the formation of ethylene in CO reduction on single-crystal copper electrodes. *J. Am. Chem. Soc.* **134**, 9864–9867 (2012).
- Jiang, K. et al. Effects of surface roughness on the electrochemical reduction of CO₂ over Cu. *ACS Energy Lett.* **5**, 1206–1214 (2020).
- Ebaid, M. et al. Production of C₂/C₃ oxygenates from planar copper nitride-derived mesoporous copper via electrochemical reduction of CO₂. *Chem. Mater.* **32**, 3304–3311 (2020).
- Wang, Y. et al. Catalyst synthesis under CO₂ electroreduction favours faceting and promotes renewable fuels electrosynthesis. *Nat. Catal.* **3**, 98–106 (2019).
- Ma, W. et al. Electrocatalytic reduction of CO₂ to ethylene and ethanol through hydrogen-assisted C–C coupling over fluorine-modified copper. *Nat. Catal.* **3**, 478–487 (2020).
- Cai, Z. et al. Selectivity regulation of CO₂ electroreduction through contact interface engineering on superwetting Cu nanoarray electrodes. *Nano Res.* **12**, 345–349 (2018).
- Li, H. et al. Changing the product selectivity for electrocatalysis of CO₂ reduction reaction on plated Cu electrodes. *ChemCatChem* **11**, 6139–6146 (2019).
- Ma, S. et al. Electroreduction of carbon dioxide to hydrocarbons using bimetallic Cu–Pd catalysts with different mixing Patterns. *J. Am. Chem. Soc.* **139**, 47–50 (2016).
- Nitopi, S. et al. Progress and perspectives of electrochemical CO₂ reduction on copper in aqueous electrolyte. *Chem. Rev.* **119**, 7610–7672 (2019).
- Zhou, Y. et al. Dopant-induced electron localization drives CO₂ reduction to C₂ hydrocarbons. *Nat. Chem.* **10**, 974–980 (2018).
- Liang, Z. Q. et al. Copper-on-nitride enhances the stable electrosynthesis of multi-carbon products from CO₂. *Nat. Commun.* **9**, 3828 (2018).
- Wang, Y. et al. Reticular chemistry in electrochemical carbon dioxide reduction. *Sci. China Mater.* **63**, 1113–1141 (2020).
- Reller, C. et al. Selective electroreduction of CO₂ toward ethylene on nano dendritic copper catalysts at high current density. *Adv. Energy Mater.* **7**, 1602114 (2017).
- Tan, D. et al. Multi-shelled CuO microboxes for carbon dioxide reduction to ethylene. *Nano Res.* **13**, 768–774 (2020).
- Karapinar, D. et al. Electroreduction of CO₂ on single-site copper-nitrogen-doped carbon material: selective formation of ethanol and reversible restructuring of the metal sites. *Angew. Chem. Int. Ed.* **58**, 15098–15103 (2019).
- Guan, A. et al. Boosting CO₂ electroreduction to CH₄ via tuning neighboring single-copper sites. *ACS Energy Lett.* **5**, 1044–1053 (2020).
- Zhao, K. et al. Selective electroreduction of CO₂ to acetone by single copper atoms anchored on N-doped porous carbon. *Nat. Commun.* **11**, 2455 (2020).
- Song, Y. et al. High-selectivity electrochemical conversion of CO₂ to ethanol using a copper nanoparticle/N-doped graphene electrode. *ChemistrySelect* **1**, 6055–6061 (2016).
- Ghodsela, T., Vesaghi, M. A., Shafiekhani, A., Baghizadeh, A. & Lameii, M. XPS study of the Cu@Cu₂O core-shell nanoparticles. *Appl. Surf. Sci.* **255**, 2730–2734 (2008).
- Espino's, J. P., Morales, J., Barranco, A., Caballero, A., Holgado, J. P. & Gonzalez-Espino, A. R. Interface effects for Cu, CuO, and Cu₂O deposited on SiO₂ and ZrO₂. XPS determination of the valence state of copper in Cu/SiO₂ and Cu/ZrO₂ catalysts. *J. Phys. Chem. B* **106**, 6921–6929 (2002).
- Wang, X. et al. Theoretical characterization of X-ray absorption, emission, and photoelectron spectra of nitrogen doped along graphene edges. *J. Phys. Chem. A* **117**, 579–589 (2013).
- Li, X. et al. Exclusive Ni–N₄ sites realize near-unity CO selectivity for electrochemical CO₂ reduction. *J. Am. Chem. Soc.* **139**, 14889–14892 (2017).
- Eilert, A., Roberts, F. S., Friebe, D. & Nilsson, A. Formation of copper catalysts for CO₂ reduction with high ethylene/methane product ratio investigated with in situ X-ray absorption spectroscopy. *J. Phys. Chem. Lett.* **7**, 1466–1470 (2016).
- Mistry, H. et al. Highly selective plasma-activated copper catalysts for carbon dioxide reduction to ethylene. *Nat. Commun.* **7**, 12123 (2016).
- Jung, H. et al. Electrochemical fragmentation of Cu₂O nanoparticles enhancing selective C–C coupling from CO₂ reduction reaction. *J. Am. Chem. Soc.* **141**, 4624–4633 (2019).
- Moller, T. et al. Electrocatalytic CO₂ reduction on CuO_x nanocubes tracking the evolution of chemical state, geometric structure, and catalytic selectivity using operando spectroscopy. *Angew. Chem. Int. Ed.* **59**, 17974–17983 (2020).
- Wang, X., Yang, D., Zuo, S., Yang, H. & Zhou, Y. Freestanding millimeter-scale porphyrin-based monoatomic layers with 0.28 nm thickness for CO₂ electrocatalysis. *Angew. Chem. Int. Ed.* **59**, 18954–18959 (2020).
- Matos, J. et al. In situ coarsening study of inverse micelle-prepared Pt nanoparticles supported on gamma-Al₂O₃: pretreatment and environmental effects. *Phys. Chem. Chem. Phys.* **14**, 11457–11467 (2012).
- Seah, M. P., Smith, G. C. & Anthony, M. T. AES—energy calibration of electron spectrometers. I—an absolute, traceable energy calibration and the provision of atomic reference line energies. *Surf. Inter. Anal.* **15**, 293–308 (1990).
- Deroubaix, G. & Marcus, P. X-ray photoelectron spectroscopy analysis of copper and zinc oxides and sulphides. *Surf. Inter. Anal.* **18**, 39–46 (1992).
- Hofmann, S. Practical surface analysis: state of the art and recent developments in AES, XPS, ISS and SIMS. *Surf. Inter. Anal.* **9**, 3–20 (1986).
- Xue, Z. H. et al. Tuning the adsorption energy of methanol molecules along Ni–N-doped carbon phase boundaries by the Mott-Schottky effect for gas-phase methanol dehydrogenation. *Angew. Chem. Int. Ed.* **57**, 2697–2701 (2018).
- Sun, Z. et al. Simultaneously realizing rapid electron transfer and mass transport in jellyfish-like Mott–Schottky nanoreactors for oxygen reduction reaction. *Adv. Funct. Mater.* **30**, 1910482 (2020).
- Cheng, T., Xiao, H. & Goddard, W. A. 3rd Full atomistic reaction mechanism with kinetics for CO reduction on Cu(100) from ab initio molecular dynamics free-energy calculations at 298 K. *Proc. Natl Acad. Sci. USA* **114**, 1795–1800 (2017).
- Thuler, M. R., Benbow, R. L. & Hurych, Z. Resonant photo- and Auger emission at the 3p threshold of Cu, Cu₂O, and CuO. *Phys. Rev. B* **26**, 669–677 (1982).
- Cai, J. et al. An APXPS endstation for gas–solid and liquid–solid interface studies at SSRF. *Nucl. Sci. Tech.* **30**, 81 (2019).
- Sculford, S. et al. Two-dimensional triangular and square heterometallic clusters: influence of the closed-shell d10 electronic configuration. *Angew. Chem. Int. Ed.* **48**, 9663–9667 (2009).
- Kruppe, C. M., Krooswyk, J. D. & Trenary, M. Selective hydrogenation of acetylene to ethylene in the presence of a carbonaceous surface layer on a Pd/Cu(111) single-atom alloy. *ACS Catal.* **7**, 8042–8049 (2017).
- Li, S.-H., Yang, Z.-X., Chen, S.-W., Lee, S.-H. & Lin, J.-L. Comparison of the chemistry of ClCH₂CH(CH₃)OH and ClCH₂CH₂CH₂OH on Cu(100) and O/Cu(100). *J. Phys. Chem. C* **120**, 9826–9835 (2016).
- Wuttig, A. et al. Tracking a common surface-bound intermediate during CO₂-to-fuels catalysis. *ACS Cent. Sci.* **2**, 522–528 (2016).
- Gunathunge, C. M., Ovalle, V. J., Li, Y., Janik, M. J. & Waegle, M. M. Existence of an electrochemically inert CO population on Cu electrodes in alkaline pH. *ACS Catal.* **8**, 7507–7516 (2018).
- Schouten, K. J. P., Pérez Gallent, E. & Koper, M. T. M. The influence of pH on the reduction of CO and CO₂ to hydrocarbons on copper electrodes. *J. Electroanal. Chem.* **716**, 53–57 (2014).
- Gao, D., Arán-Ais, R. M., Jeon, H. S. & Roldan Cuenya, B. Rational catalyst and electrolyte design for CO₂ electroreduction towards multicarbon products. *Nat. Catal.* **2**, 198–210 (2019).
- Fan, L., Xia, C., Zhu, P., Lu, Y. & Wang, H. Electrochemical CO₂ reduction to high-concentration pure formic acid solutions in an all-solid-state reactor. *Nat. Commun.* **11**, 3633 (2020).

52. Xu, H. et al. Highly selective electrocatalytic CO₂ reduction to ethanol by metallic clusters dynamically formed from atomically dispersed copper. *Nat. Energy* **5**, 623–632 (2020).
53. Yoo, J. S., Christensen, R., Vegge, T., Norskov, J. K. & Studt, F. Theoretical insight into the trends that guide the electrochemical reduction of carbon dioxide to formic acid. *ChemSusChem* **9**, 358–363 (2016).
54. Liu, C. et al. Single-boron catalysts for nitrogen reduction reaction. *J. Am. Chem. Soc.* **141**, 2884–2888 (2019).
55. Liu, M. et al. Enhanced electrocatalytic CO₂ reduction via field-induced reagent concentration. *Nature* **537**, 382–386 (2016).
56. Lin, S. C. et al. Operando time-resolved X-ray absorption spectroscopy reveals the chemical nature enabling highly selective CO₂ reduction. *Nat. Commun.* **11**, 3525 (2020).
57. Jiang, Z. L. et al. Discovery of main group single Sb-N₄ active sites for CO₂ electroreduction to formate with high efficiency. *Energy Environ. Sci.* **13**, 2856–2863 (2020).
58. Chen, C. et al. Coupling N₂ and CO₂ in H₂O to synthesize urea under ambient conditions. *Nat. Chem.* **12**, 717–724 (2020).
59. Su, X. Z. et al. Operando spectroscopic identification of active sites in NiFe Prussian Blue analogues as electrocatalysts: activation of oxygen atoms for oxygen evolution reaction. *J. Am. Chem. Soc.* **140**, 11286–11292 (2018).

Acknowledgements

This work was financially supported by the Photon Science Center for Carbon Neutrality, National Natural Science Foundation of China (Grant No. 11975301, 21801015, and 2210020315), Beijing Institute of Technology Research Fund Program for Young Scholars (3090012221909), Youth Innovation Promotion Association of the Chinese Academy of Sciences (2020286), Shanghai Synchrotron Radiation Facility Operation Research Project, Maintenance and reconstruction project for large scientific equipment of Chinese Academy of Sciences and National Major Scientific Research Instrument Development Project (41827802), Users with Excellence program of Hefei Science Center of CAS(2020HSC-UE003) and the Fundamental Research Funds for the Central Universities (WK2310000099). The authors thank the BL02B and 03U in the Shanghai Synchrotron Radiation Facility (SSRF), BL01B in the National Synchrotron Radiation Laboratory (NSRL) for help with characterizations. The authors thank Experimental Center of Advanced Materials (ECAM) of School of Materials Science & Engineering, Beijing Institute of Technology for help with characterizations. We are grateful to Chuangwei Liu and Jige Chen for valuable discussions, support, and cooperation of DFT calculations. We thank Yang Liu, Guoqiang Chen and Li Ma for helpful discussions on this work. The authors thank Big Data Science Center of Shanghai Synchrotron Radiation Facility. This work was also supported by Experimental Supporting System at Shanghai Synchrotron Radiation Facility. The authors also thank Analytical Instrumentation Center (#SPST-AIC10112914) (SPST, ShanghaiTech University), the Electron Microscopy Center and the HPC Platform of ShanghaiTech University and Beijing Zhongkebaice Technology Service Co., Ltd.

Author contributions

Y.W., D.W., and W.C. conceived the project and designed the experiments. Y.W. and X.S. performed the *operando* XAS experiments, EXAFS data analysis and XANES simulations. X.S., H.L., and Z.Q. performed the *operando* SR-FTIR experiments and data analysis. Z.P. and F.Y. designed Quasi-in situ XPS and AES experiments. X.S., X.N., and Z.P. performed the Quasi-in situ XPS and AES experiments and data analysis. Z.J. and W.C. conducted material synthesis. Z.J., D.Z., H.S., and W.C. performed structural characterization. J.Z. carried out DFT calculations. Y.W., X.S. W.C., and Z.J. wrote the manuscript. X.S. and Y.W. provided interpretation of mechanism. All authors discussed the results and commented on the manuscript.

Competing interests

The authors declare no competing interests.

Additional information

Supplementary information The online version contains supplementary material available at <https://doi.org/10.1038/s41467-022-29035-8>.

Correspondence and requests for materials should be addressed to Wenxing Chen or Yu Wang.

Peer review information *Nature Communications* thanks the anonymous reviewers for their contribution to the peer review of this work.

Reprints and permission information is available at <http://www.nature.com/reprints>

Publisher's note Springer Nature remains neutral with regard to jurisdictional claims in published maps and institutional affiliations.



Open Access This article is licensed under a Creative Commons Attribution 4.0 International License, which permits use, sharing, adaptation, distribution and reproduction in any medium or format, as long as you give appropriate credit to the original author(s) and the source, provide a link to the Creative Commons license, and indicate if changes were made. The images or other third party material in this article are included in the article's Creative Commons license, unless indicated otherwise in a credit line to the material. If material is not included in the article's Creative Commons license and your intended use is not permitted by statutory regulation or exceeds the permitted use, you will need to obtain permission directly from the copyright holder. To view a copy of this license, visit <http://creativecommons.org/licenses/by/4.0/>.

© The Author(s) 2022